EPFL

Semester Project - Fall 2025

# Solar 4L

Florentin Julien

Supervisors : Kléber NICOLET-DIT-FELIX, Antonin FAES
Professor : Christophe BALLIF


Figure 1: Implementation on the car of the module

## Contents

# 1 Abstract

This work presents the design, fabrication, and testing of a compact photovoltaic energy system integrated into a mobile battery pack for automotive use. A high-efficiency homemade PV module with SunPower cells was developed and characterized, with electroluminescence and IV curve tests confirming its electrical and mechanical integrity. Energy conversion is managed through an MPPT controller, while dedicated DC-DC converters supply USB and 12 V loads with properly tuned PI controllers. Battery management relies on a $LiFePO_4$ pack with state-of-charge estimation implemented via current integration and an Extended Kalman Filter. The system demonstrates reliable energy production, conversion, and storage, offering a portable solution for mobile renewable energy applications.

# 2 Introduction

This project originates from the desire to make a Renault 4L participating in the 4L Trophy more environmentally friendly and modern. The goal is to integrate a photovoltaic system on the car's roof to provide supplementary energy while improving the monitoring of the vehicle's operation. By adding solar panels, energy can be harvested for auxiliary loads without relying solely on the engine, thus reducing fuel consumption and environmental impact during the rally.
In addition to energy generation, the system incorporates sensors and monitoring devices embedded in the car. On one side, sensors supervise the engine's operations, while on the other, they monitor the photovoltaic system, verifying energy production, conversion efficiency, and battery behavior. This dual monitoring approach enables a comprehensive assessment of the vehicle's energy performance.
The project specifically targets the 4L Trophy rally in February, where the car will be subjected to real-world conditions, including varying sunlight, terrain, and load demands. The design integrates energy harvesting, storage, conversion, and intelligent monitoring in a compact, portable battery pack, demonstrating the feasibility of augmenting traditional vehicles with renewable energy systems in a practical and competitive context.

# 3 Objectives

The primary objectives of this project are as follows:

- Design and fabricate a high-efficiency photovoltaic module suitable for mobile deployment.
- Implement maximum power point tracking (MPPT) to maximize energy extraction from the PV module.
- Develop and test DC-DC conversion circuits for fan cooling and USB loads, and a single-phase AC inverter for higher voltage loads.
- Characterize and manage a $LiFePO_4$ battery pack with state-of-charge estimation, ensuring safe and efficient operation.
- Integrate all components into a portable battery pack capable of interfacing with a vehicle's existing systems and providing real-time monitoring.
- Evaluate system performance under realistic operating conditions and provide recommendations for future improvements.

# Sizing of the system and its parameters

## 4 Optimisation of the overall system

### 4.1 Optimization of the solar cell types and disposition

The choice and disposition of the solar cell in the module is of primary importance in this project as the roof's surface is limited and we want to capture the maximum amount of energy. From the measurements, the car's roof has available flat surface of around $1m \times 1m$. In order to allow a proper fixation of the module on the roof, it was therefore chosen to make the module around $90cm \times 90cm$.
For this situation, several kind of solar cell types have been investigated. As the surface area of the module is small, the choice of the solar cell type highly depended on their theoretical efficiency which are summarized in table 1.

| Cell type | Power per unit of surface $[W/m^2]$ |
|---|---|
| Poly-Si | 160 – 180 |
| Mono-PERC | 190 – 210 |
| SunPower | 220 – 240 |

Table 1: Solar cell theoretical efficiency comparison [1] [2]

From the table 1, it was chosen to use SunPower solar cells. Their dimensions are : $12.5cm \times 12.5cm$. Due to the maximum module size ($90cm \times 90cm$), the maximum number of cells per row/column is : 90/12.5 = 7.2 cells meaning we can set a grid of 7x7 cells on the module, which generates a module of $87.5cm \times 87.5cm$. Then, we need to also take into account some spaces in between the cells, this distance is set by the connector used and can be considered to be $2.3mm$. A margin on the ribbons edges of $25mm$ and a margin of $15mm$ on the other sides also has to be considered.
From all these considerations, the module would contain 49 cells with a dimension of $92cm \times 94cm$, would produce $170 - 180Wp$ with a $V_{oc} = 36V$ and $I_{sc} = 5.9A$. Thanks to the low breakdown voltage of SunPower cells, the risk of hot spots under shaded conditions are avoided. However to improve the yield efficiency, we decided to include some bypass diodes. For this goal, one bypass diode has been inserted at the end of each row to avoid power loss and reduce the risk of shading. Figure 2 correctly defines the module shape with the dimensions and the solar cell arrangement.

### 4.2 Choice of the battery

#### 4.2.1 Daily energy production estimation

To estimate the daily energy production of the photovoltaic module during the planned journey, we used PVGIS simulations [3] for representative locations along the route. For February, Biarritz was chosen as an example of low solar availability, while Algeciras and Marrakech were considered for locations with higher irradiance according to figure 3.

Then, with the same software, one can compute the average daily energy production of the given solar panel in the correct locations :

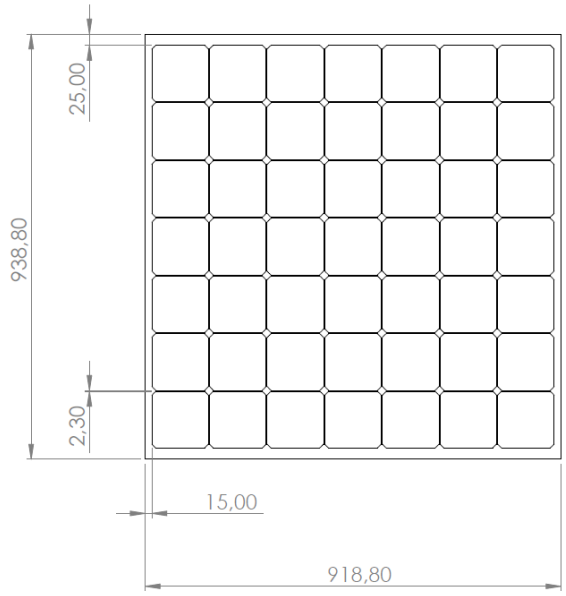


Figure 2: Solar cell arrangement on the module

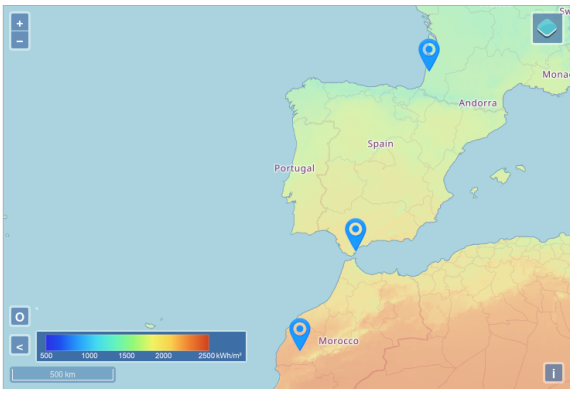


Figure 3: Map of the journey with the irradiance.

- **Biarritz (France, 2 days in February / 1 day in March):** production of 267 Wh/day in February and 392 Wh/day in March.
- **Algeciras (Spain, 6 days in February):** production of 377 Wh/day in February and 496 Wh/day in March.
- **Marrakech (Morocco, 3 days in February):** production of 512 Wh/day in February and 633 Wh/day in March.

From these results, Biarritz represents the lowest-sun conditions, while Marrakech provides the highest solar availability. This allows us to select representative cities for the energy estimation and define *equivalent days* for the journey.

To compute the average daily energy production over the entire journey, we use a weighted average based on the number of days in each location:

$$E_{\text{avg}} = \frac{2\times 267 + 1\times 392 + 6\times 377 + 3\times 512}{2+1+6+3} = \frac{534+392+2262+1536}{12} = \frac{4724}{12} \approx 393\,\text{Wh/day}.$$

Thus, the system can be expected to produce on average approximately 390–395 Wh per day, corresponding to roughly 2.3 hours of equivalent full sun per day.

To avoid excessive cycling and ensure battery longevity, the battery should not be discharged below 30% of its total capacity. Based on the estimated average daily energy production of about 393 Wh, the minimum battery capacity should satisfy:

$$E_{\text{bat,min}} = \frac{E_{\text{avg}}}{1-0.3} \approx \frac{393}{0.7} \approx 561\,\text{Wh}.$$

### 4.2.2 Identification of the suitable battery

Based on the daily energy production estimation, the photovoltaic system requires a battery capable of storing at least 560 Wh while maintaining a minimum state-of-charge of 30%. Several factors were considered in selecting the appropriate battery: nominal voltage, capacity, weight, cost, and compatibility with the MPPT controller.
Depending on the system design and desired cost/weight trade-offs, different nominal voltages can be considered:

- **12 V:** minimum 50 Ah to satisfy energy requirements. Two practical options were identified:
  - Solution 1: two 12.8 V, 20 Ah batteries in parallel (2.5 kg each)
  - LFP battery with BMS: 12 V, 50 Ah, maximum charge current 40 A (4.5 kg), allowing direct connection to PV without a DC/DC converter
- **24 V:** minimum 25 Ah, could use higher-voltage batteries such as electric bike packs
- **48 V:** minimum 12.5 Ah, generally less practical for small systems

Two main chemistries were considered: lithium iron phosphate ($LiFePO_4$, LFP) and valve-regulated lead-acid (VRLA) [4]:

- **VRLA:** slower charging due to 0.25 C limit, can charge down to −20°C, lower energy density (100 Wh/L or 40 Wh/kg), typical cost around 200 $/kWh, 500–3000 cycles.
- **LFP:** high charge current capability (no C-rate limitation), cannot charge below 0°C, higher energy density (250 Wh/L or 150 Wh/kg), higher cost (≃400 $/kWh) but 2000–4000 cycles.

Given the requirements of this project, including the need for lightweight, compact storage, and compatibility with the MPPT controller, LFP batteries are the preferred choice. The higher upfront cost is offset by longer lifetime, higher energy density, and faster charging, which is critical for maximizing energy harvested during short solar exposure periods.
Considering the daily energy production estimates, the desired nominal system voltage, and the advantages of lithium iron phosphate ($LiFePO_4$) chemistry, the battery selected for this project is a **12 V $LiFePO_4$ battery with approximately 640 Wh of usable capacity** [5]. This capacity exceeds the estimated minimum requirement of 560 Wh, providing a safety margin that reduces depth-of-discharge and extends battery lifetime. The 12 V format is directly compatible with the chosen MPPT controller and simplifies system integration, while the $LiFePO_4$ chemistry offers high energy density, good charge/discharge efficiency, and a long cycle life, making it well suited for use in a mobile photovoltaic system.

## 4.3 Choice of the Solar Controller

The electrical power delivered by a photovoltaic module strongly depends on its operating point, which is determined by the connected load and varies with irradiance and temperature. To ensure that the PV module operates as close as possible to its maximum power point (MPP) under all conditions, a solar charge controller is required. Two controllers are commonly used in photovoltaic systems: Pulse Width Modulation (PWM) and Maximum Power Point Tracking (MPPT).

A PWM controller directly couples the PV module to the battery, forcing the module voltage to follow the battery voltage. As a result, the PV module rarely operates at its maximum power point, leading to

significant power losses, especially when the optimal module voltage is higher than the battery voltage. In contrast, an MPPT controller continuously adjusts the operating voltage of the PV module through a DC–DC conversion stage in order to extract the maximum available power. This capability allows the MPPT controller to adapt to variations in environmental conditions and to fully exploit the electrical characteristics of high-efficiency photovoltaic cells [6]. This situation is explained in details in figure 4.

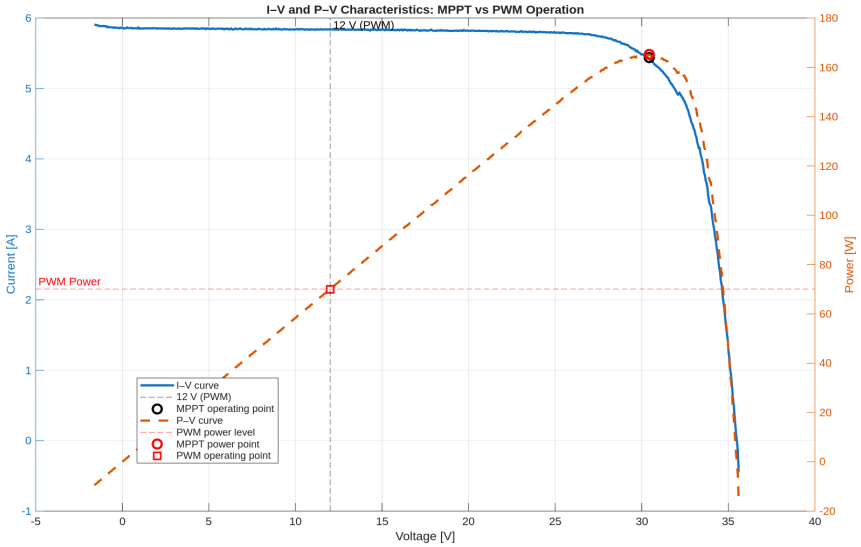


Figure 4: MPPT vs PWM example behaviour on a I-V curve.

Given the limited available surface area for the PV module and the use of high-efficiency SunPower cells, maximizing the energy harvested per unit area is a key design objective. Under these constraints, the use of an MPPT controller is clearly preferable to a PWM-based solution, as it significantly improves the overall energy yield and system efficiency.

Once the choice of an MPPT architecture is established, selecting an appropriate MPPT controller becomes a critical step in the system design. The characteristics of the MPPT controller, including its input voltage range, conversion efficiency, power handling capability, and tracking algorithm, must be carefully matched to the electrical characteristics of the PV module and the requirements of the energy storage system in order to ensure optimal performance of the complete system.

From the previous sections, the maximum power produced by the PV module is close to $180W$. As the battery operates in 12V the charging current can reach 15A. On the PV side, the electrical characteristics of the module indicate a maximum open circuit voltage of 36V and a short-circuit current of 6A. The MPPT controller therefore has to be able to handle these values.
Two main approaches were considered to meet these requirements: the design of a custom MPPT demonstrator board or the use of a commercially available MPPT controller. While a custom solution would offer greater flexibility, it would significantly increase design complexity, development time, and cost, without providing enough benefits for a system operating at this relatively low power level. Given the availability, reliability, and cost-effectiveness of commercial solutions, the use of an off-the-shelf MPPT controller was therefore identified as the most appropriate choice for this project.
Among commercially available low-power MPPT controllers, the BlueSolar MPPT 75/15 was selected. This controller supports PV input voltages up to 75V and a maximum charging current of 15A, making it well suited to handle the approximately 200W generated by the PV module while charging a 12V battery. Its specifications ensure safe operation under all expected operating conditions and allow the system to fully exploit the available photovoltaic power.
In addition to its electrical capabilities, a key advantage of the BlueSolar MPPT is its open communication interface, which allows direct data exchange with the controller. This feature enables monitoring, data logging, and control of the MPPT, facilitating system diagnostics and integration with external de-

vices for enhanced experimentation and system management.

# 5 Battery management

Reliable battery management is a critical aspect of the photovoltaic system. Neither the battery nor the MPPT controller provides a direct estimation of the battery state of charge (SoC). However, knowledge of the SoC is essential for safe operation and energy management. Consequently, a dedicated SoC estimation strategy was developed and implemented.

## 5.1 Motivation and Challenges

For lithium iron phosphate ($LiFePO_4$) batteries, the open-circuit voltage (Voc) is directly related to the state of charge and can, in theory, be used to estimate SoC. However, in practice, the battery is almost always under load or charge, meaning that Voc cannot be directly measured. Instead, only the terminal voltage is available, which is affected by internal resistive and dynamic effects.
Furthermore, the Voc–SoC characteristic is relatively flat over a wide operating range (approximately 20–80% SoC), making voltage-based estimation highly sensitive to measurement noise and modeling errors, see figure 5.

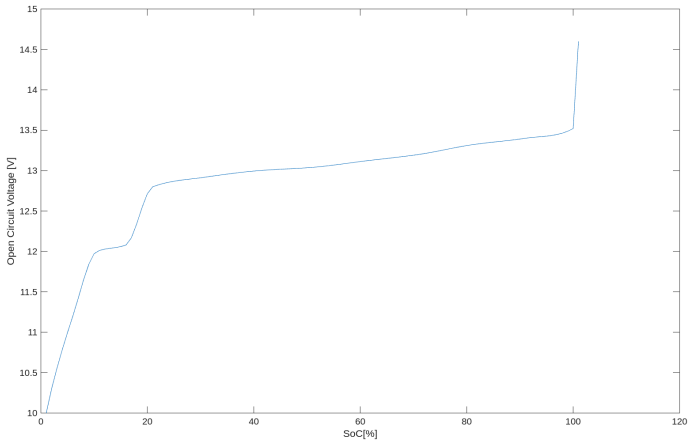


Figure 5: Open circuit voltage of a $LiFePO_4$ battery against State of Charge [7].

## 5.2 Battery Modeling

To estimate the internal battery voltage and SoC under load, an equivalent electrical model was developed based on the literature [8, 9, 10]. The battery is modeled as an ideal voltage source $E$ (Voc) in series with an ohmic resistance $R$ and $n$ parallel RC networks accounting for dynamic behavior. In this work, $n = 3$ was selected to accurately capture the battery dynamics.
The terminal voltage is expressed as:

$$V = E + RI + \sum_{i=1}^{n} V_i$$

with V the measured voltage at the battery's terminal, E the internal cell voltage and I the measured current at the battery's terminal. This convention assumes discharge current to be positive.

Each RC branch voltage follows the discrete-time state equation:

$$V_i(k) = a_i V_i(k-1) + b_i I(k)$$

with

$$a_i = \exp\left(-\frac{\Delta t}{\tau_i}\right), \qquad b_i = (1 - a_i) R_i$$

where $\tau_i$ and $R_i$ are the time constants and resistance of the $i$-th RC branch. The model parameters were identified experimentally using current and voltage measurements. See Appendix B for the details on the development of these constants.

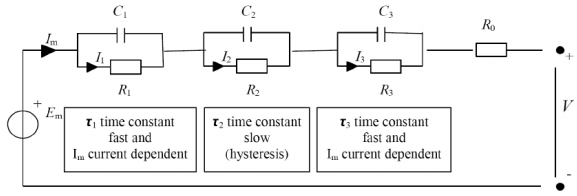


Figure 6: Three RC battery model [11].

## 5.3 SoC Estimation Approaches

Once the battery parameters are identified, the internal voltage $E$ can be estimated from measurements of terminal voltage and current. In principle, this voltage can then be mapped to SoC using the known Voc-SoC relationship. However, due to the flat slope of this relationship over most of the operating range, this method is highly sensitive to noise and parameter uncertainty, making it unreliable on its own.

A simpler and commonly used method is current integration (coulomb counting), defined as:

$$\mathrm{SoC}(t) = \mathrm{SoC}(0) + \frac{1}{Q_{nom}} \int_0^t I(\tau)\, d\tau$$

This method requires an accurate initial SoC and precise current measurements. In practice, determining the initial SoC is challenging because a true open-circuit condition is needed to estimate Voc. Due to the long time constants of the battery model, a rest period of several minutes (typically 5-10 minutes) is required before the internal voltage stabilizes, which is not always feasible in a real system.

## 5.4 Extended Kalman Filter Approach

To overcome the limitations of voltage-based and pure current-integration methods, an Extended Kalman Filter (EKF) was implemented for state-of-charge estimation. The EKF builds upon the identified battery model and augments it with a recursive state estimation framework that combines model-based prediction with measurement correction.
The EKF state vector is defined as:

$$\mathbf{x}(k) = \begin{bmatrix} \mathrm{SoC}(k) & V_1(k) & V_2(k) & V_3(k) \end{bmatrix}^T$$

where SoC is the state of charge and $V_i$ are the voltages across the RC branches of the equivalent battery model. The system dynamics are given by:

$$\mathrm{SoC}(k+1) = \mathrm{SoC}(k) + \frac{\Delta t}{Q_{\mathrm{nom}}} I(k)$$

$$V_i(k+1) = a_i V_i(k) + b_i I(k)$$

with:

$$a_i = \exp\left(-\frac{\Delta t}{\tau_i}\right), \quad b_i = (1 - a_i) R_i$$

The output equation relates the measured terminal voltage to the states:

$$V(k) = E(\mathrm{SoC}(k)) + RI(k) + \sum_{i=1}^{3} V_i(k)$$

where $E$(SoC) is the open-circuit voltage obtained from the experimentally identified Voc–SoC curve. The battery parameters were identified experimentally using current excitation and voltage measurements. The resulting values are summarized below:

- Ohmic resistance: $R_s = 0.329\Omega$
- RC branch resistances: $R_1 = 0.1399\Omega$, $R_2 = 0.0726\Omega$, $R_3 = 23.244\Omega$
- Time constants: $\tau_1 = 0.717s$, $\tau_2 = 5.363s$, $\tau_3 = 9.993 \cdot 10^4 s$

These parameters allow accurate reconstruction of the terminal voltage dynamics and were used consistently in both simulation and EKF implementation. These parameter have been tested over different tests of charging and discharging of the battery and can be visualized in figure 7. The computed Root Mean Square Error (RMSE) of each dataset with the reconstructed terminal voltage is below 0.5 V while the voltage range from 8 to 13 V which depicts the fact that the model captures the system dynamic.

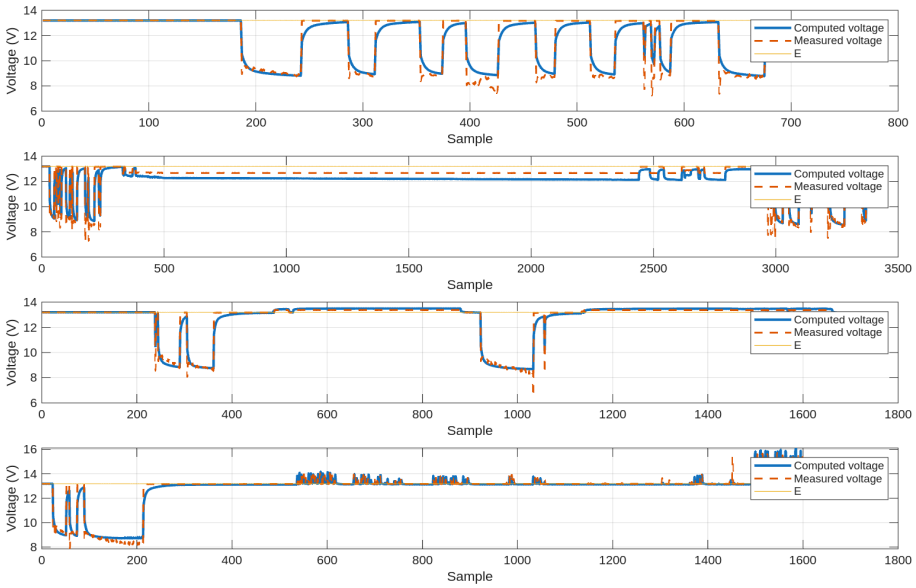


Figure 7: Estimation of the terminal voltage using the computed parameters and internal voltage of the battery over four different test of charging and discharging of the battery. E is the open circuit voltage of the battery, measured voltage corresponds to the terminal voltage of the battery and computed voltage corresponds to the terminal voltage of the battery computed from the open circuit voltage. For dataset 1 RMSE is 0.50 V, for dataset 2 RMSE is 0.47 V, for dataset 3 RMSE is 0.21 V and for dataset 4 RMSE is 0.36 V

At each time step, the EKF first predicts the next state using the nonlinear state equations. The predicted terminal voltage is then computed and compared to the measured voltage. The estimation error is used to update the state vector through the Kalman gain, which is computed from the linearized measurement Jacobian.
Due to the relatively flat slope of the Voc–SoC characteristic between 20% and 80% SoC, the sensitivity of the output voltage to changes in SoC is low in this region. As a result, the Jacobian terms associated with SoC become small, and the EKF correction relies primarily on current integration. This explains why the EKF converges toward results similar to coulomb counting in the mid-SoC range.

Near the operating boundaries (high or low SoC), the Voc–SoC slope increases significantly, leading to higher sensitivity of the voltage measurement to SoC variations. In these conditions, the EKF provides improved convergence and better correction of accumulated integration errors compared to pure coulomb counting.

### 5.4.1 Linearization and Jacobian Computation

Since the battery model and the open-circuit voltage function $E(\text{SoC})$ are nonlinear, the Extended Kalman Filter relies on local linearization of the state and measurement equations. At each time step, the nonlinear functions are linearized around the current state estimate using first-order Taylor expansion.

The state-transition Jacobian matrix is defined as:

$$\mathbf{F}(k) = \frac{\partial f}{\partial \mathbf{x}} = \begin{bmatrix} 1 & 0 & 0 & 0 \\ 0 & a_1 & 0 & 0 \\ 0 & 0 & a_2 & 0 \\ 0 & 0 & 0 & a_3 \end{bmatrix}$$

The measurement Jacobian matrix is given by:

$$\mathbf{H}(k) = \begin{bmatrix} \frac{\partial E(\text{SoC})}{\partial \text{SoC}} & 1 & 1 & 1 \end{bmatrix}$$

where $\frac{\partial E(\text{SoC})}{\partial \text{SoC}}$ is obtained from the slope of the experimentally identified Voc–SoC curve. These Jacobians are used to compute the Kalman gain and update the state estimate and covariance matrix at each iteration.

## 5.5 Simulation and Validation

The different SoC estimation methods were implemented and tested in MATLAB/Simulink. The results include voltage reconstruction, SoC estimation accuracy, and convergence behavior for both current integration and EKF-based approaches. A charging test of the battery has been performed and the State of Charge estimation computed using Coulomb's counting method and the EKF method are displayed in figure 8. Both of them have the same predictions as expected.

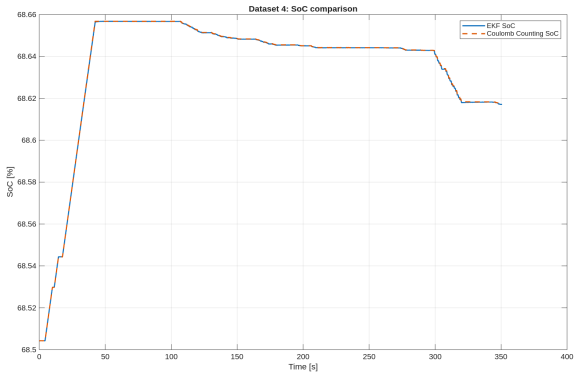


Figure 8: EKF and Coulomb's counting estimation of the State of Charge of the battery during a charging step of the battery

# 6 Sizing of the converters

The energy harvested from the photovoltaic system must be handled and modifed before being used to power the loads or charge the battery. In this project, three different power converters are connected to the output of the MPPT controller, each serving a specific purpose:

- A **PWM-controlled fan** to regulate the temperature of the battery and electronics, ensuring safe operation.
- A **DC-DC buck converter** to step down the battery voltage to 5 V for USB ports and low-voltage loads.
- A **single-phase inverter** to convert 12 V DC into 220 V AC at 50 Hz for standard AC appliances.

This section presents the sizing of these converters, including the selection of components, calculation of required ratings, and simulation results that validate the design choices. Each converter is analyzed separately, with its respective electrical requirements and design parameters.

## 6.1 PWM Fan Controller

The 12 V BLDC fan is used to maintain the battery and electronics within an optimal temperature range. A cascaded control structure is implemented. A linear control logic is implemented for fan speed, where the fan remains off below 20°C, ramps linearly between 20°C and 45°C, and runs at maximum speed above 45°C. This outer loop generates a reference fan speed.

The inner loop regulates the fan speed using a PI controller, converting the speed reference $\omega^\star$ into a PWM duty cycle. Temperature measurements are obtained using a DHT11 sensor at a sampling rate of 0.5 Hz, which is sufficient given the slow thermal dynamics of the system. The inner speed control loop operates at 1 kHz to ensure fast dynamic response. The PWM carrier frequency is set to 10 kHz in order to reduce audible noise and electrical disturbances caused by the internal commutation of the BLDC fan, while maintaining good energy efficiency. The overall control structure is shown in Figure 9.

From this reference fan speed, the inner loop then regulates the fan speed using a PI controller converting the speed reference into a PWM duty cycle. Temperature measurements are obtained using a DHT11 sensor at a rate of 0.5 Hz, which is sufficient given the slow thermal dynamics of the system. The inner loop operates at 1 kHz to ensure fast dynamic response. The PWM carrier frequency is set to 10kHz in order to reduce audible electrical noise caused by the internal commutation of the BLDC fan while maintaining good energy efficiency. The full control system can be visualized in figure 9.

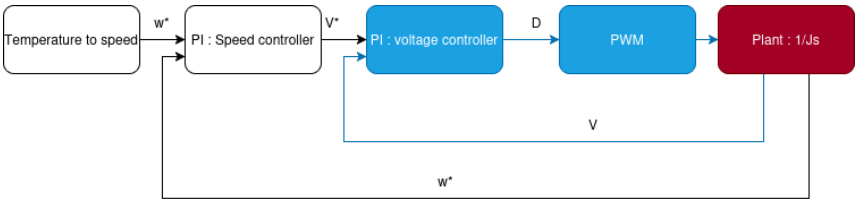


Figure 9: Control scheme of the temperature regulator. Black arrows indicate the outer loop, blue arrows are the inner loop and the red box is the plant.

The fan plant can be approximated as a pure integrator with transfer function $T(s) = J\dot{\omega}$, where $J$ is the rotor inertia. Using the *symmetrical optimum method* for tuning a pure integrator, the inner loop PI controller has the form:

$$C(s) = \frac{1 + sT_n}{sT_i}, \quad T_n = 4T_{pE}, \quad T_i = \frac{8T_{pE}^2}{J}$$

where $T_{pE}$ is the plant delay (approximately $2T_s$, with $T_s$ being the sampling time) and $J$ is the moment of inertia ($J = \frac{1}{2}mr^2 \approx 2 \times 10^{-6}\,\mathrm{kg\,m^2}$). The outer loop PI controller has been tuned using This tuning provides stable and responsive temperature regulation for the fan.

The fan is powered through a high-side NMOS transistor, with a bulk input capacitor and a bypass diode for current smoothing and protection. The fan consumes a maximum of 2 W, corresponding to a maximum current draw of approximately 340 mA. The system can be visualized in the figure 10.

The control logic allows smooth ramping of the fan speed and precise thermal regulation of the system. Figure 19 shows a step response simulation from Simulink, demonstrating the fan speed response to a temperature step input.

## 6.2 DC-DC Buck Converter (12V to 5V)

The DC-DC buck converter supplies 5 V for USB ports and low-voltage electronics from the 12 V battery. It is designed for a maximum load power of 20 W, corresponding to a maximum current of 4 A at 5 V.

The converter consists of:

- High-side NMOS transistor for switching

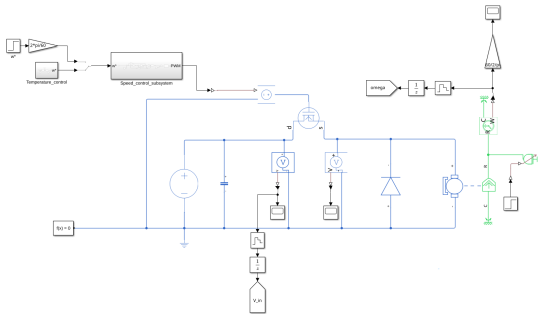

Figure 10: Simulink electrical schematic of the FAN control

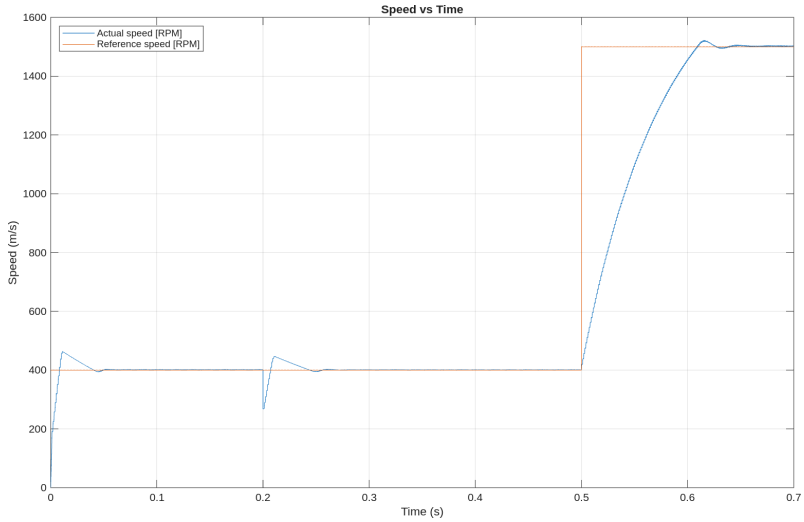


Figure 11: Simulated step response of the PWM fan controller. Step of fan speed from 400RPM to 1500RPM at $t = 0.5s$ and load change on the fan propeller at $t = 0.2s$.

- Bulk input capacitor for voltage smoothing
- LC output filter with $L = 80\,\mu$H and $C = 40\,\mu$F

It can be visualized in figure 12.

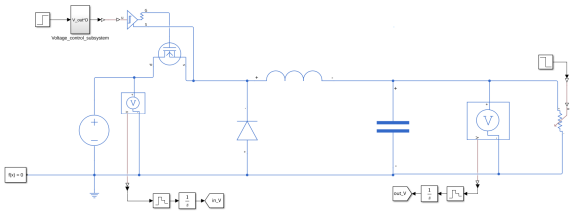

Figure 12: Simulink electrical schematic of the Buck control

The switching PWM operates at $f_s = 18\,$kHz, while the voltage control loop runs at 1 kHz. A maximum current protection is implemented to prevent overloading the converter.

The inductor is sized using:

$$\Delta I_L = \frac{(V_{in} - V_0)DT_s}{L} \quad \Rightarrow \quad L = \frac{(V_{in} - V_0)DT_s}{\Delta I_L}$$

with $\Delta I_L = 5\% I_c$ (load current $I_c = 4\,$A) and duty cycle $D \approx 5/12$.

The output capacitor is sized to limit voltage ripple:

$$C = \frac{\Delta I_L}{8 f_s \Delta V_0}$$

with $\Delta V_0 = 500\,\text{mV}$.

The voltage loop is implemented as a PI controller. The controller ensures stable regulation under varying battery voltage and load conditions. As the dominant dynamics of the power stage can be approximated by a pure integrator, the plant transfer function is modeled as:

$$\frac{I_L(s)}{V_L(s)} = \frac{1}{Ls}$$

where $L$ is the output inductor. Given this integrator behavior, the *symmetrical optimum* tuning method was selected for the controller design. This approach is well suited for systems dominated by integral dynamics and allows a good compromise between stability margins and dynamic response.
Using this method, the PI controller parameters were tuned to account for the converter delay and the sampling frequency of the voltage loop. The resulting controller ensures fast voltage regulation with limited overshoot and stable behavior under load transients. Simulation results in Simulink confirm the effectiveness of this tuning strategy.

Figure 13 shows the Simulink simulation results including load step and reference voltage step. The output ripple in voltage corresponds to the $\Delta V_0 = 0.5V$ used for the sizing of the elements.

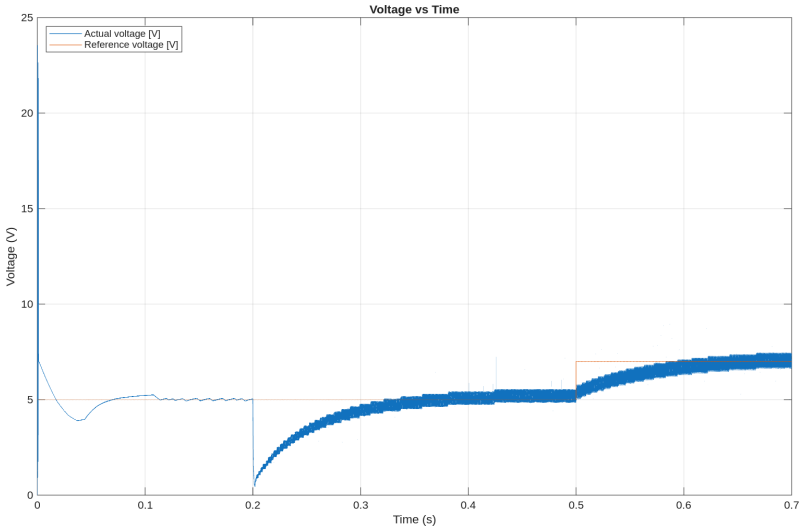


Figure 13: Simulink simulation of the DC-DC buck converter. Step in the load characteristic at $t = 0.2s$ and step in voltage reference from 5V to 7V at $t = 0.5s$.

## 6.3 Single-phase DC-AC converter (12V to 220V 50Hz)

A single-phase inverter is used to convert the 12 V DC battery voltage into a 220 V RMS, 50 Hz AC output suitable for standard AC loads. The inverter is controlled by an ESP microcontroller, which generates PWM signals to drive a full-bridge power stage composed of four NMOS transistors.

The inverter consists of a full-bridge DC–AC converter operating with a PWM frequency of 10 kHz. The bridge output is connected to a high-frequency transformer that steps up the voltage from 12 V to 220 V. The transformer output is followed by an LC filter to reconstruct a low-distortion sinusoidal voltage at 50 Hz. An additional LC filter is placed between the battery and the inverter input to limit current

ripple and reduce electromagnetic disturbances fed back to the battery.

Due to the single-phase nature of the inverter, advanced control strategies such as $dq$-frame control are not applicable. Therefore, a voltage-only control strategy is implemented. The output voltage is regulated using a PI controller, ensuring accurate tracking of the 220 V RMS reference at 50 Hz.

The control gains are derived from the theoretical formulation of the outer voltage loop commonly used in three-phase inverters. These gains were adapted to the single-phase case and validated through simulation. The voltage control loop is updated at 100 Hz, which is sufficient for regulating a 50 Hz sinusoidal output.

Output voltage and current measurements are performed using an INA sensor. Due to the sensor's maximum sampling frequency of 2 kHz, a sampling rate of 1 kHz was selected. To accurately extract the fundamental 50 Hz component of the signal, a low-pass digital filter is applied to the measured data. This approach provides stable and reliable feedback for the voltage control loop.

The output LC filter is designed to attenuate the PWM switching harmonics while preserving the fundamental frequency. A cutoff frequency of approximately 100 Hz was selected. Based on this requirement, the following component values were chosen:

$$L = 80\,\mu\text{H}, \qquad C = 3\,\mu\text{F}$$

$$f_c = \frac{1}{2\pi\sqrt{LC}}$$

These values provide effective harmonic attenuation while maintaining acceptable dynamic response. A similar LC filter is also used at the inverter input to limit current ripple drawn from the battery.

The complete inverter system, including the full-bridge, transformer, LC filters, and control loops, was modeled in Simulink. Figure 14 presents the simulation schematic, while Figure 15 shows the output voltage response to a reference step. The results demonstrate stable operation, correct voltage regulation, and low distortion of the 50 Hz output waveform.

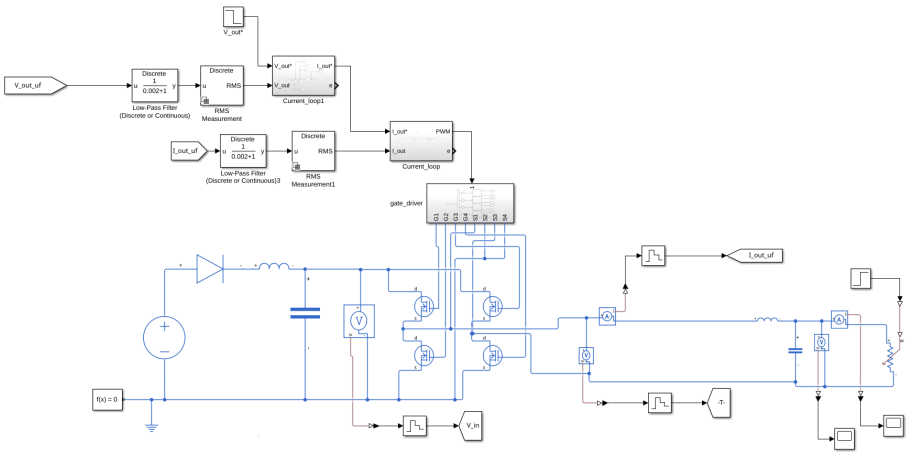


Figure 14: Simulink model of the single-phase DC–AC inverter.

## 6.4 Summary and production of the PCB

The different power converters designed in this section were integrated into a single power electronics system connected to the MPPT load output. The overall architecture includes a PWM-controlled fan

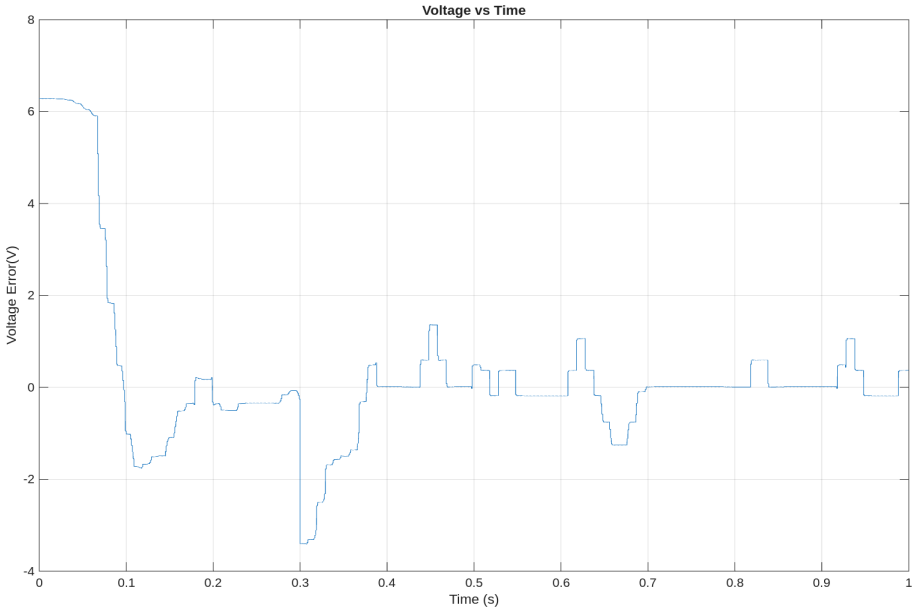


Figure 15: Error between reference voltage and output voltage of the inverter when voltage reference has step from 220V to 110V at $t = 0.3s$.

for thermal management, a DC-DC buck converter for low-voltage loads, and a single-phase DC–AC inverter for AC power generation.

The complete system schematic and the PCB layout are presented in Appendix A.

# Test in normal conditions

## 7 Solar module testing

This section presents the validation tests performed on the photovoltaic module under normal conditions. The objective of these tests is to verify the electrical integrity of the module after assembly and to assess its performance relative to the expected theoretical values.

### 7.0.1 Module Architecture and Assembly Verification

As described in the previous section, the photovoltaic module is composed of 49 SunPower cells arranged in 7 rows of 7 cells in series. Each row was manufactured and tested individually prior to final module assembly.
To verify both the electrical quality of the cells and the integrity of the soldering process, each string was inspected using an electroluminescence (EL) test. This method consists of injecting a current into the cell string and observing the emitted infrared radiation, which is proportional to carrier recombination within the cells. The EL inspection allows detection of cracked cells, broken interconnections, and soldering defects. During this step, one defective solder joint was identified and corrected before proceeding further.
Once validated, the cell strings were laid out, interconnected, and equipped with bypass diodes located at the end of each string to mitigate partial shading effects. The complete stack was then prepared for lamination. The module structure is composed of multiple functional layers, combining electrical insulation, mechanical stiffness, and environmental protection. A schematic cross-section of the photovoltaic module layers is provided in Figure 16.

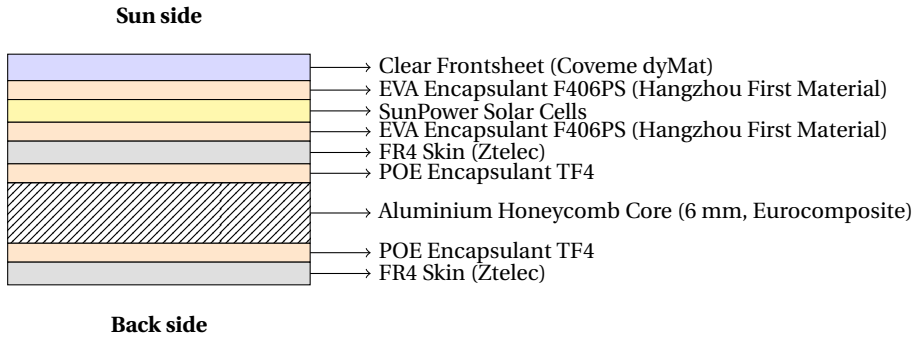


Figure 16: Cross-sectional schematic of the photovoltaic module showing the layered material stack used during fabrication.

The materials used for the module fabrication are listed below:

- Frontsheet: dyMat Clear Frontsheet Monolayer (Coveme)

- Encapsulant (front): EVA F406PS (Hangzhou First Material)
- Encapsulant (rear): POE TF4 (Hangzhou First Material)
- Structural skins: FR4 sheets (Ztelec)
- Core material: 6 mm aluminium honeycomb (Eurocomposite)

Module before lamination can also be visualized in Appendix C.
After lamination mechanical integration steps were carried out. Holes were drilled through the laminated stack and reinforced using threaded inserts to allow secure mounting on the vehicle. Junction boxes were soldered to the module terminals and bonded to the rear side of the panel. An aluminum frame was finally added to ensure mechanical rigidity, edge protection, and ease of handling.

A second electroluminescence test was performed on the fully assembled module (see Figure 17). The results show uniform emission across the majority of the cells, indicating consistent electrical behavior. One cell exhibits a visible crack; however, current continuity is preserved. Minor non-emissive spots are also observed on a few cells, but these remain localized and do not significantly affect the overall module performance.

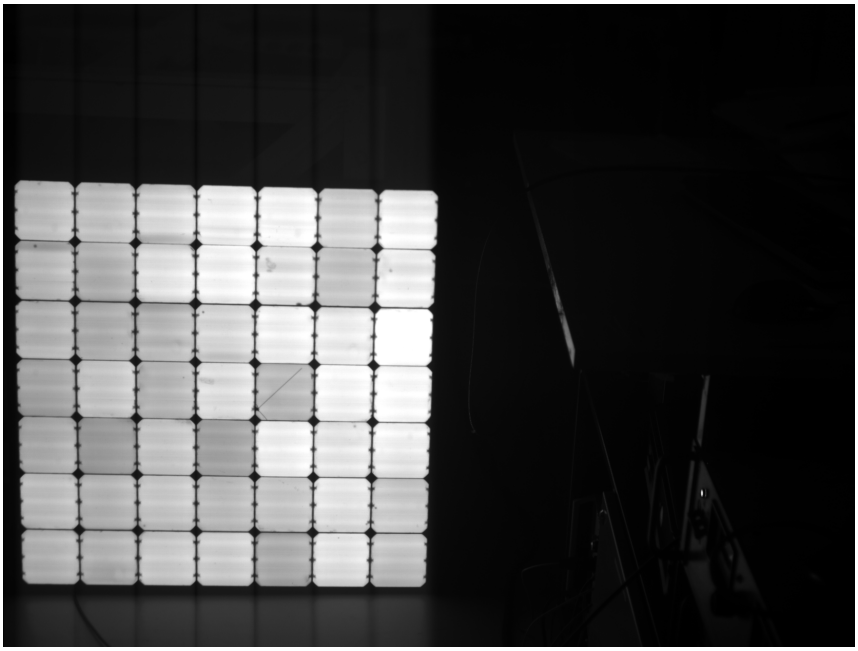

Figure 17: Electroluminescence image of the fully assembled photovoltaic module.

### 7.0.2 I–V Characterization and Performance Validation

Following assembly and EL validation, the module was characterized using a PASAN solar simulator under Standard Test Conditions (STC). The resulting current–voltage (I-V) and power–voltage (P-V) curves are shown in Figure 18.

The key measured parameters are summarized below:

- Open-circuit voltage: $V_{oc} = 35.49\,V$
- Short-circuit current: $I_{sc} = 5.86\,A$
- Maximum power point voltage: $V_{mp} = 30.42\,V$
- Maximum power point current: $I_{mp} = 5.44\,A$
- Maximum power: $P_{max} = 165.3\,W$

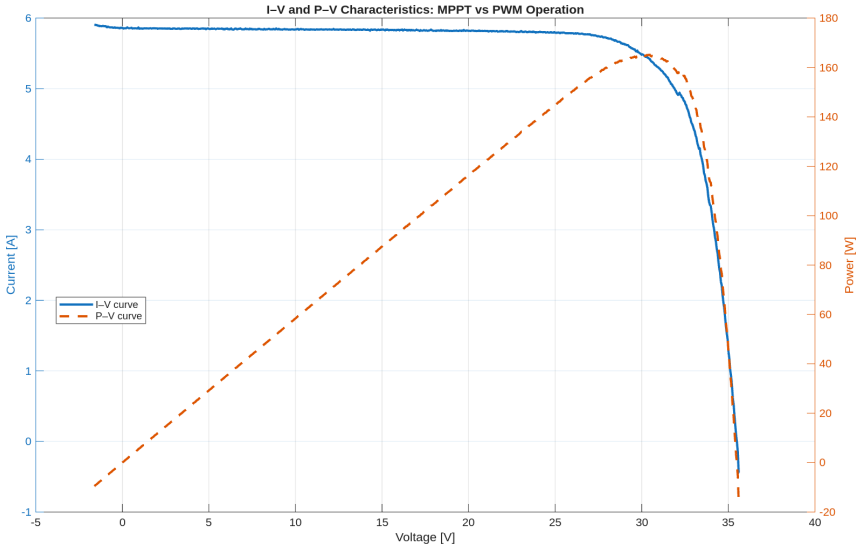


Figure 18: Measured I–V and P–V curves of the photovoltaic module under STC.

- Fill factor: 79.5%
- Module temperature: 21.4°$C$

From a theoretical standpoint, the expected values for the module were approximately $V_{oc} \approx 36$V and $I_{sc} \approx 5.9$A. The measured results are in very good agreement with these predictions, with deviations well within typical manufacturing tolerances and measurement uncertainty.

Overall, the electrical characterization confirms that the module operates as intended, with no significant degradation introduced during the assembly process. The consistency between theoretical expectations, electroluminescence inspection, and I–V measurements validates the suitability of the module for integration into the complete photovoltaic system.

# 8 Converters testing

This section presents the experimental and simulation-based validation of the DC converters connected to the MPPT load output. At this stage of the project, two converters were fully tested: the battery cooling fan controller and the DC–DC buck converter used to generate a regulated 5 V supply. The single-phase inverter is therefore not addressed in this section.

The objective of these tests is to verify the correct dynamic behavior of the controllers under realistic operating conditions and to confirm consistency with the control design presented in the previous sections.

### 8.0.1 Fan Controller Validation

The fan controller is designed to regulate the thermal environment of the battery pack and power electronics. As described previously, the control strategy consists of a linear open-loop speed reference between 20 °C and 45 °C, followed by a closed-loop PI controller acting on the fan speed. Above 45 °C, the fan operates at maximum speed.
To validate the controller behavior, a temperature step was applied to the system, corresponding to a simulated increase of the battery pack temperature from 20 °C to 40 °C. The resulting fan speed response is shown in Figure 19.

The controller exhibits a short delay corresponding to the control loop dynamics and some limitation of the physical system; the fan does not rotate when voltage is below 4V corresponding to a duty cy-

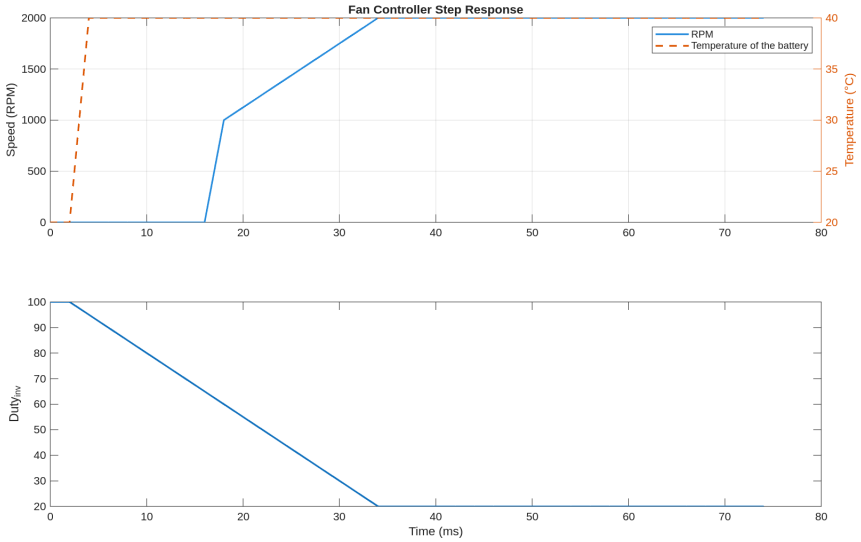


Figure 19: Fan controller step response to temperature increase

cle above 70%. The fan speed then increases smoothly, following the imposed linear temperature–speed relationship, before reaching a steady-state operating point. No oscillations or instability are observed, and the response time is consistent with the selected PI tuning and sampling rates.

This behavior confirms that the fan controller is capable of mitigating temperature increases in a controlled manner, ensuring sufficient cooling to the battery pack.

### 8.0.2 DC–DC Buck Converter Validation

The DC-DC buck converter is designed to provide a regulated 5 V supply from the 12 V battery for auxiliary loads such as USB ports. The converter operates with a PWM switching frequency of 18 kHz and a voltage control loop updated at 1 kHz. A current limitation mechanism is also implemented to protect the converter and connected loads.
To assess the dynamic performance of the voltage controller, a step change in the output voltage reference from 3 V to 5 V was applied. The corresponding output voltage response is presented in Figure 20.

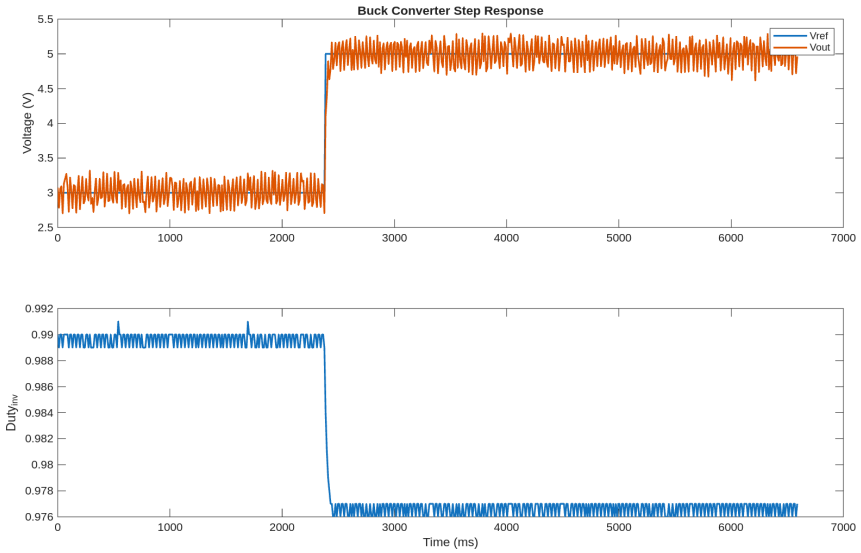


Figure 20: Voltage controller step response to voltage demand increase.

The measured response is in good agreement with the theoretical expectations derived from the control design. The $\Delta V$ peak-to-peak is below the computed 0.5 V, and the settling time is short, indicating a well-damped system. No sustained oscillations are observed, and the converter quickly converges to the new reference value.

# 9 Implementation on the car

The complete photovoltaic energy system was integrated into a dedicated, transportable battery pack designed for on-vehicle operation. The objective of this implementation was to ensure safe, modular, and reliable operation while enabling real-time monitoring and data acquisition during driving and stationary phases.

### 9.0.1 Battery Pack Architecture

All electrical and control components are housed within a single enclosure forming the battery pack. A detailed view of the battery pack and its internal components is provided in Appendix D. The enclosure contains the battery, the MPPT charge controller, the DC-DC converters and the cooling fan. The mechanical design allows the pack to be easily transported, installed, and removed from the vehicle.

The power distribution interface provides multiple user-accessible outputs:

- Two USB-C ports for high-power DC loads,
- Two USB-A ports for standard 5 V devices,
- One 12 V DC outlet,
- One 220 V AC outlet supplied through the inverter,
- For security reason, it also includes a hardware emergency button.

### 9.0.2 Monitoring and Control System

In order to supervise the operation of the photovoltaic system and evaluate its performance in real conditions, a dedicated monitoring and data visualization interface was developed. This interface runs on a Raspberry Pi and collects measurements from the different subsystems of the vehicle, including the photovoltaic module, the battery pack, and the power converters.

The monitored quantities include the PV module voltage and current, instantaneous power production, battery voltage, current and estimated state of charge, as well as environmental measurements such as module temperature and solar irradiance. These data allow real-time assessment of the energy production, conversion efficiency, and thermal behavior of the system.

The interface provides a centralized view of the system state and can be accessed directly during operation of the vehicle. It is used both for validation purposes during testing phases and for supervision during normal operation, enabling rapid identification of abnormal behavior or performance degradation. A screenshot of the monitoring interface is provided in Figure 21.

This centralized monitoring capability allows the user to assess system performance at a glance and facilitates debugging and post-analysis through logged data. The server contains some display options and let the user the possibity to analyze time series while the system is running.

### 9.0.3 Sensors and Performance Monitoring

Additional sensors were integrated into the system to assess environmental and operating conditions. A temperature sensor is used to monitor the PV module temperature, enabling the evaluation of thermal

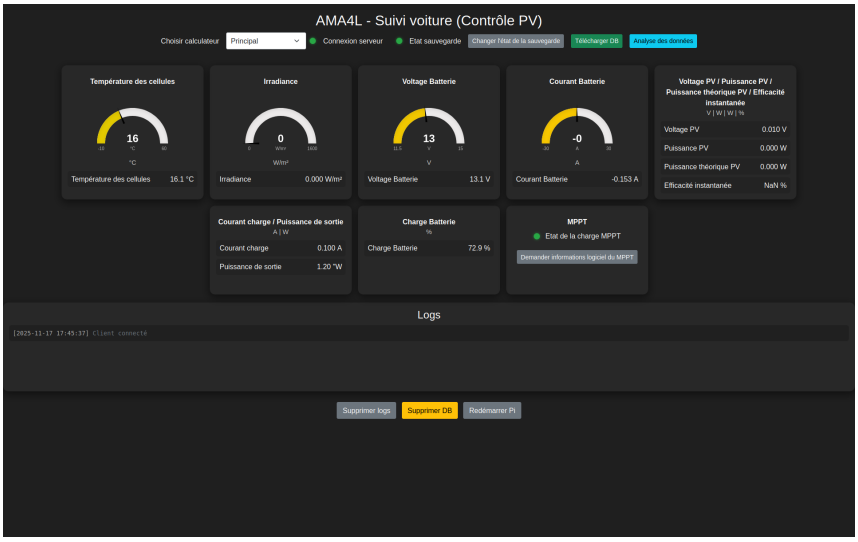


Figure 21: Raspberry Pi graphical interface displaying system measurements.

effects on performance. An irradiance sensor measures the incident solar radiation, allowing comparison between expected and actual energy production and providing a direct means to assess module efficiency under real operating conditions.

These measurements are continuously recorded by the Raspberry Pi and can be correlated with electrical data to analyze system behavior in varying environmental conditions.

### 9.0.4 Integration with Vehicle Supervision

The Raspberry Pi is also capable of communicating with the vehicle's engine supervision controller. This communication enables coordinated monitoring of both the photovoltaic energy system and the vehicle's propulsion system.

# Discussion

## 10 Discussion and Conclusion

This project demonstrated the design, fabrication, and testing of a compact photovoltaic energy system for automotive use. The SunPower-based PV module performed close to theoretical expectations, with electroluminescence and IV curve tests confirming both mechanical and electrical integrity. The MPPT controller proved essential, extracting more energy than a PWM approach, while the DC-DC converters for fan and USB loads showed reliable operation with properly tuned PI controllers.

Battery management was a critical challenge. Voltage-based estimation proved insufficient in the mid-SoC range due to the flat Voc–SoC characteristic of $LiFePO_4$ batteries. Coulomb counting and an Extended Kalman Filter were implemented; the EKF showed improved robustness at the charge boundaries, though performance was similar to integration in normal operation.
The complete system was successfully integrated into a portable battery pack, including monitoring, fan cooling, and USB/12V/220V outputs. Limitations remain with the AC inverter, which could not be fully tested.

Future work could focus on commissioning the AC inverter, extending field testing, and refining SoC estimation with adaptive methods. Overall, this work demonstrates the feasibility of integrating high-efficiency PV generation, energy conversion, and battery management into a compact mobile system, providing a solid foundation for further development.

# 11 Appendix

## A Power Electronics Schematics and PCB Layout

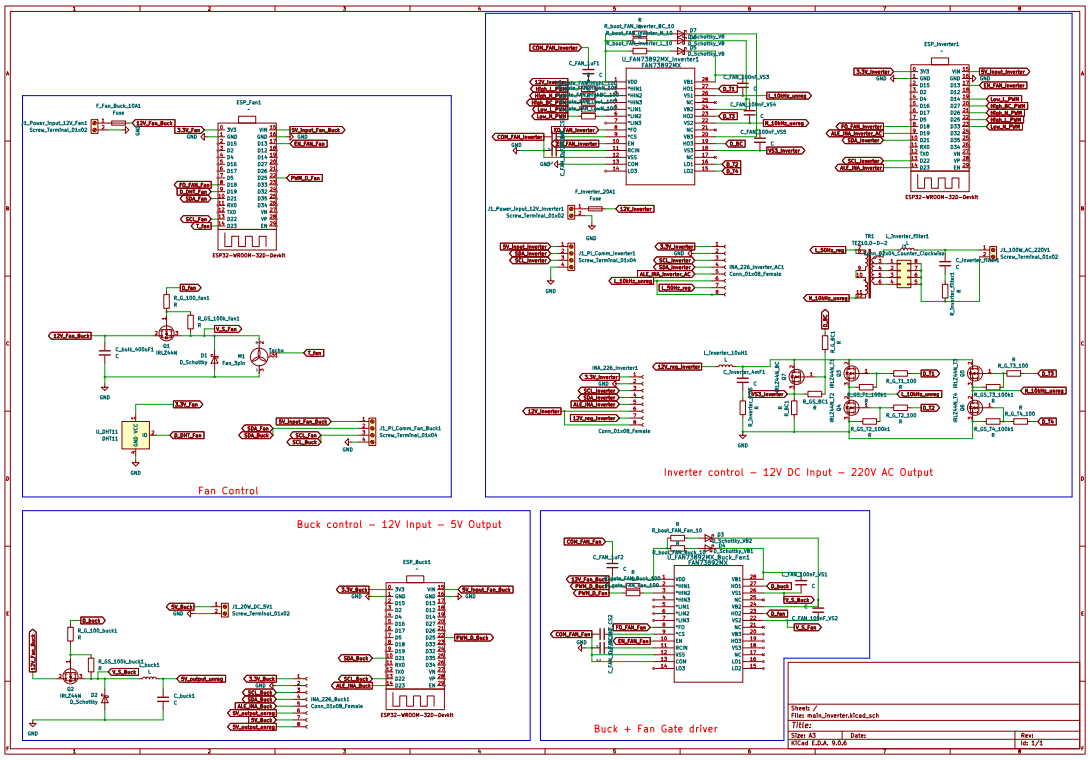


Figure 22: Global schematic of the photovoltaic energy management system.

## B Derivation of the Battery RC Model Discretization

This appendix derives the discrete-time state equations used for the RC branches of the battery equivalent circuit and justifies the expressions of the coefficients $a_i$ and $b_i$.
Each RC branch of the battery model consists of a resistance $R_i$ in parallel with a capacitor $C_i$. The voltage across the capacitor is denoted $V_i(t)$. Applying Kirchhoff's laws to the $i$-th RC branch yields the continuous-time differential equation:

$$C_i \frac{dV_i(t)}{dt} + \frac{V_i(t)}{R_i} = I(t) \Rightarrow \frac{dV_i(t)}{dt} = -\frac{1}{R_i C_i} V_i(t) + \frac{1}{C_i} I(t) = -\frac{1}{\tau_i} V_i(t) + \frac{R_i}{\tau_i} I(t)$$

with $tau_i = R_i C_i$.
Assuming that the current $I(t)$ is constant over one sampling interval $\Delta t$, the solution of the differential equation over the interval $[k\Delta t, (k+1)\Delta t]$ is:

$$V_i(k+1) = e^{-\frac{\Delta t}{\tau_i}} V_i(k) + \left(1 - e^{-\frac{\Delta t}{\tau_i}}\right) R_i I(k)$$

This yields the discrete-time state equation:

$$V_i(k+1) = a_i V_i(k) + b_i I(k)$$

with:

$$a_i = \exp\left(-\frac{\Delta t}{\tau_i}\right), \qquad b_i = (1 - a_i) R_i$$

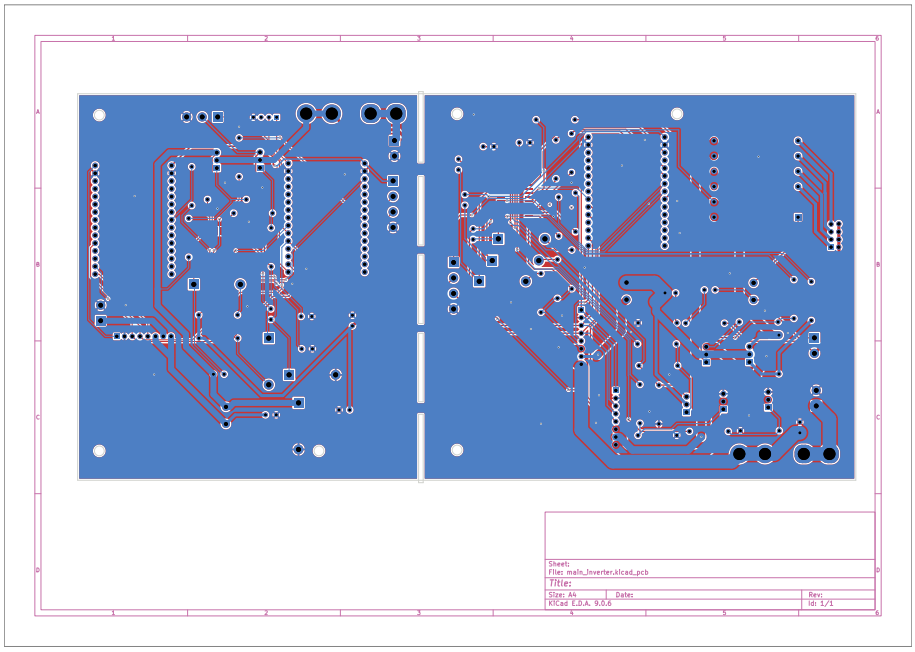

Figure 23: PCB layout of the power electronics board.

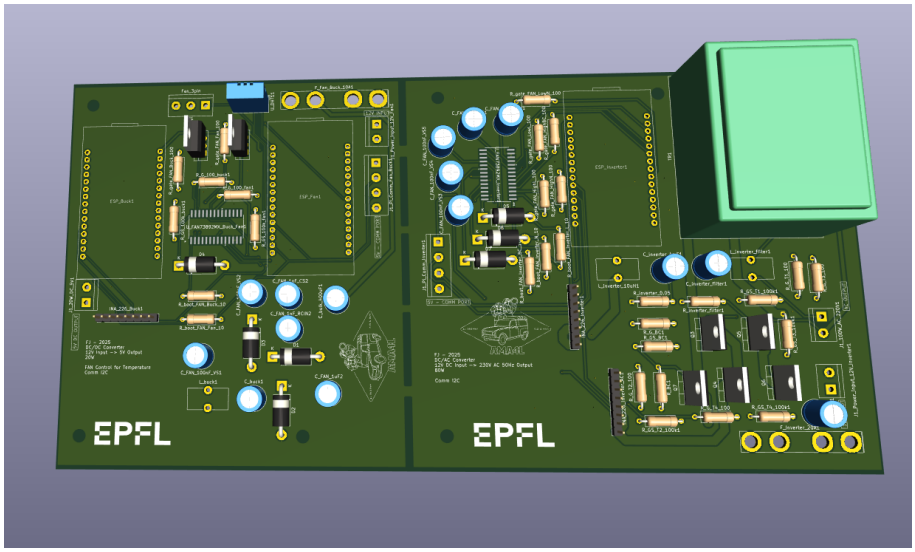


Figure 24: 3D PCB view with components of the three controllers

# C Module preparation

# D Hardware Implementation

# E Vehicle Integration

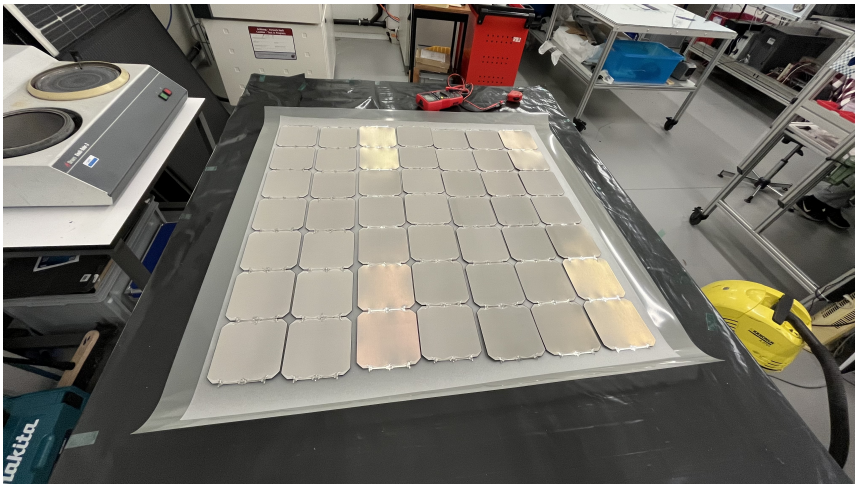

Figure 25: Layout of the cells and different layers before lamination of the module.

Figure 26: Aluminum frame around the module

## References

[1] Maxeon Solar Technologies, "Ibc technology — maintaining performance leadership," https://corp.maxeon.com/static-files/c5e8e15e-b191-4bab-96ff-cec504040019, 2025, accessed: 2025-09-18.

[2] Clean Energy Reviews, "Most efficient solar panels 2025," https://www.cleanenergyreviews.info/blog/most-efficient-solar-panels, 2025, accessed: 2025-09-18.

[3] "Pvgis – photovoltaic geographical information system," https://re.jrc.ec.europa.eu/pvg_tools/en/tools.html, European Commission, Joint Research Centre, accessed: 2025-09-18.

[4] H. Keshan, J. Thornburg, and T. S. Ustun, "Comparison of lead-acid and lithium ion batteries for stationary storage in off-grid energy systems," in *4th IET Clean Energy and Technology Conference (CEAT 2016)*, 2016, pp. 1–7.

[5] "12 v lifepo$_4$ lithium battery," https://fr.anern.net/12v-lifepo4-lithium-battery, AnErn, accessed: 2025-09-18.

Figure 27: Connection port on the back side of the module

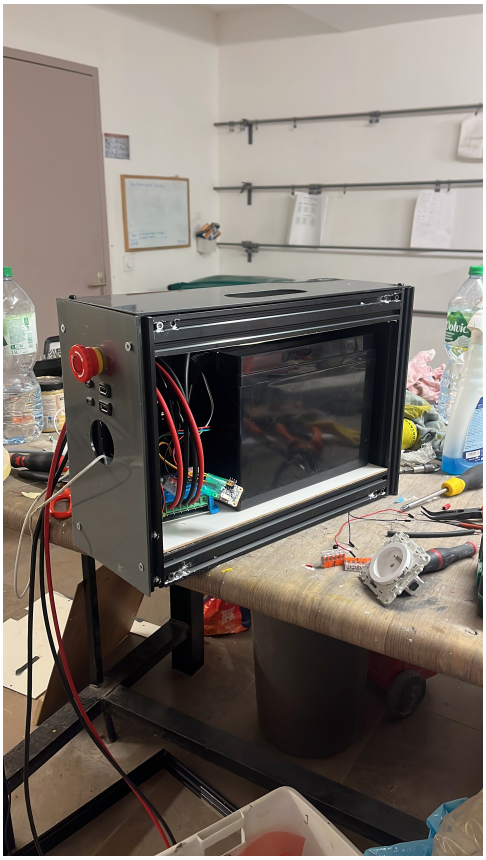

Figure 28: Battery pack integrating the battery, MPPT controller, converters, and cooling system.

[6] A. Yılmaz, A. Demirci, and S. M. Tercan, "Technical comparison of pwm and mppt charge regulators," in *2021 13th International Conference on Electrical and Electronics Engineering (ELECO)*, 2021, pp. 78–83.

[7] "Lifepo4 voltage chart," https://cleversolarpower.com/lifepo4-voltage-chart/, Clever Solar Power, accessed: 2025-10-10.

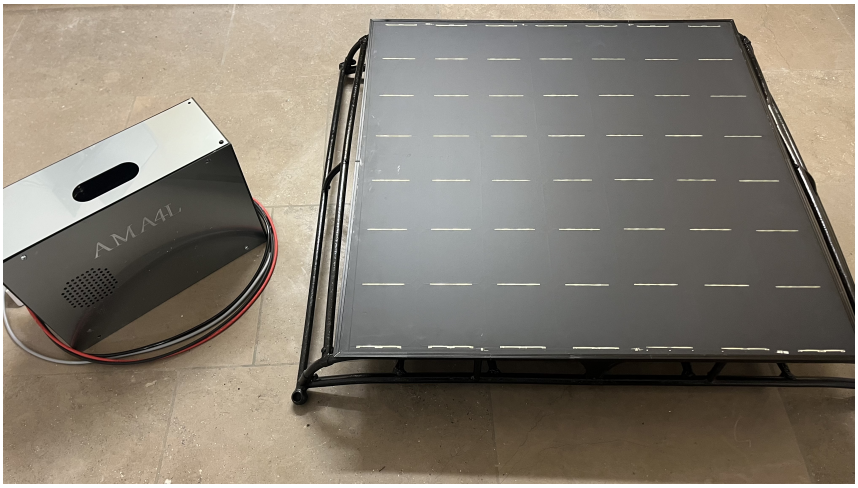

Figure 29: Battery pack with the PV module attached on its support

[8] R. Benedikt, B. Simon, and T. Blank, "Implementing an extended kalman filter for soc estimation of a li-ion battery with hysteresis: A step-by-step guide," *energies*, 2021.

[9] Z. Cui, W. Hu, G. Zhang, Z. Zhang, and Z. Chen, "An extended kalman filter based soc estimation method for li-ion battery," *Energy Reports*, vol. 8, pp. 81–87, 2022, iCPE 2021 - The 2nd International Conference on Power Engineering. [Online]. Available: https://www.sciencedirect.com/science/article/pii/S2352484722003638

[10] A. Maheshwari, S. Nageswari, R. Palanisamy, B. Karthikeyan, M. M. Mahmoud, D. E. M. Wapet, A. M. El-Rifaie, E. Touti, and A. I. Omar, "Real-time parameter identification and state of charge estimation of electric vehicle batteries," *Engineering Reports*, vol. 7, no. 8, p. e70346, 2025. [Online]. Available: https://onlinelibrary.wiley.com/doi/abs/10.1002/eng2.70346

[11] T. Huria, R. Jackey, J. Gazzarri, M. Saginaw, and P. Sanghvi, "Battery model parameter estimation using a layered technique: An example using a lithium iron phosphate cell," vol. 2, 04 2013.